Effect of Er and Zr additions and aging treatment on grain refinement of aluminum alloy fabricated by laser powder bed fusion

DOI:
10.1016/j.jallcom.2022.165237

Document Version
Accepted author manuscript

Effect of Er and Zr additions and aging treatment on grain refinement of aluminum alloy fabricated by laser powder bed fusion

Yanwu Guo [a], Wu Wei [a] *, Wei Shi [b], Bo Zhang [a], Xiaorong Zhou [c], Shengping Wen [a], Xiaolan Wu [a], Kunyuan Gao [a], Li Rong [a], Hui Huang [a], Zuoren Nie [a] *

[a] Key Laboratory of Advanced Functional Materials, Education Ministry of China, Beijing University of Technology, Beijing 100124, China

[b] Institute of Corrosion Science and Technology, Guangzhou 510530, China

[c] School of Materials, The University of Manchester, Manchester, M13 9PL, UK

* Corresponding author, Address: Key Laboratory of Advanced Functional Materials, Education Ministry of China, Beijing University of Technology, Beijing 100124, China.

E-Mail address: weiwu@bjut.edu.cn (Wu Wei), zrnie@bjut.edu.cn (Zuoren Nie)

Abstract

In this work, Al-0.88Er-0.78Zr (wt.%) alloy was fabricated via laser powder bed fusion (LPBF). The microstructure, precipitates distribution, electrical conductivity and hardness of as-built and aging treatment specimens were carefully characterized. Results show that LPBF process greatly expand the solid solubility of Er and Zr in Al. The addition of Er can significantly refine the grain size and form a bimodal grain structure consisting of fine equiaxed grains (grain size ~0.53 ± 0.15 μm) at the boundary of molten pool together with coarse columnar grains (width 2.57 ± 0.84 μm) at the center of molten pool. After 375 ℃ for 3 h aging treatment, the particles on the grain boundary inhibit the grain growth; at the same time, a large number of $Al_3(Er,Zr)$ particles with $L1_2$ structure and size of 2.25 ± 0.3 nm are precipitated, which plays a major role in enhancing the hardness with the peak hardness of about 89.24 ± 3.77 HV. Er and Zr elements are proved to be an alternative way of the additive elements for developing a new 3D printing high-strength aluminum alloy.

Keywords: Aluminum; Laser powder bed fusion; Erbium; Bimodal grain structure; Precipitation

1. Introduction

Additive manufacturing technology, also known as 3D printing, can rapidly fabricate components with complex geometry through the principle of layer-by-layer. Compared with conventional manufacturing methodologies, additive manufacturing

technology can save a lot of materials and time [1]. Being a kind of additive manufacturing technology, laser powder bed fusion (LPBF) uses laser as heat source and metal powder as feedstock. Because the molten pool is relatively small (hundreds of microns) and cooling rate is very fast (10^{3-6} K/s) [2], the samples prepared by LPBF have higher dimensional precision and more excellent mechanical properties than those prepared by traditional casting or other additive manufacturing technologies, such as laser directed energy deposition (L-DED) [3].

There are many kinds of aluminum alloy materials, which are widely used in aerospace, transportation, mechanical construction and other fields. However, columnar grain structures are obtained in aluminum alloy fabricated by LPBF process under the influence of the high temperature gradient and cooling rate [4]. On the one hand, the columnar grains have larger grain size, and tend to trigger anisotropy properties [5]; on the other hand, for wrought Al alloys, especially 2xxx, 6xxx and 7xxx high-strength aluminum alloys, the high concentration of alloy elements and the wide solidification range lead to the formation of hot cracking at the columnar grain boundaries [6]. The small equiaxed semi-solid structure could produce the rotation and deformation of the grains so as to absorb strain, which could not only suppress the cracking [6], but also refine grain size to improve the mechanical properties, such as tensile strength, fatigue strength and elongation [7]. Therefore, it is expected to obtain equiaxed grain structure or equiaxed-columnar bimodal grain structure in the Al alloys fabricated by LPBF. Bimodal grain structure has been proved to be an effective strategy for circumventing the strength–ductility trade-off [8]. However, due to high temperature gradient, it is hard to realize columnar-to-equiaxed transition (CET) behavior by adjusting the process parameters. The most effective way to obtain the fine grain structure is to adjust the composition of alloy elements, promoting the heterogeneous nucleation by introducing nucleation particles [9]. Zr has been widely used as heterogeneous nucleation element. Here are some examples: 7075 aluminum alloy powder were coated with 1 vol% hydrogenstabilized zirconium nucleants, using an electrostatic assembly technique [6]; 2 vol% Yttrium Stabilized Zirconia (YSZ) was added to an Al6061 base powder by means of a dry mixing procedure [10]; Al-Cu-Mg powder mixture with 2 wt.% Zr particles were blended by mechanical mixing [11], forming a large number of equiaxed grains at the boundary of the molten pool in the above researches, which refines the grain size and suppresses hot cracking.

In order to improve the strength of aluminum alloy, it is required that the alloy

elements also have precipitation strengthening effect during the aging process. Croteau et al. [12] found that in Al-3.66Mg-1.57Zr (wt.%) alloy manufactured by LPBF process, sub-micrometer Al_3Zr particles are precipitated to act as nucleation sites and refine the grain size, and the precipitation of nano-size $L1_2$-Al_3Zr particles during subsequent aging, leads to an increase in strength [13]. Compared with Zr element, Sc also has the effect of grain refinement, and the secondary Al_3Sc precipitates have more significant precipitation strengthening effect [14]. More importantly, composite alloying of Sc and Zr can further improve precipitation strengthening and thermal stability due to the formation of Al_3(Sc,Zr) precipitates [15]. Subsequently, INSPIRE-AG and its collaborators developed Al-4.6Mg-0.66Sc-0.42Zr alloy [16], and Jia et al. [17] studied Al-4.52Mn-0.79Sc-0.74Zr alloy. Both alloys have good comprehensive tensile properties in the effect of solution strengthening, grain boundary strengthening, and precipitation strengthening. Unfortunately, the price of Sc is so expensive (about $6500 / kg [18]) that the price of Al-Mg-Sc-Zr powder is several times higher than that of Al-Si powder. Researchers tried to reduce the concentration of Sc in Al alloy: Li et al. [19] studied Al-8.0Mg-1.3Si-0.5Mn-0.5Sc-0.3Zr alloy; Bi et al. [18] found that the Al-14Mg-0.47Si-0.31Sc-0.17Zr alloy fabricated by LPBF can still achieve high mechanical properties by adding appropriate amount of Si, even if the Sc content is decreased. Therefore, it is necessary to find cheap and effective alloy elements with the same effect as Sc, which can not only refine grain size but also provide precipitation strengthening effect.

The price of Er is more competitive than Sc. It has been also found that Al–Er is a promising system capable of precipitation strengthening [20], and has a certain grain refinement effect [21, 22]. Meanwhile, Er–Zr composite alloying shows synergetic effect due to the precipitation of Al_3(Er,Zr) nano-particles with $L1_2$ structure [23]. Unfortunately, the solid solubility of Er in Al is 0.045 at% during the conventional solidification situation, which is only 1/5 of Sc, resulting in a limited increment of strength in Al–Er alloy [24]. Laser rapid solidification could expand the solid solubility of solute elements in the matrix [25]. Jia et al. [26] found that laser remelting improves the hardness of the Al-Er-Zr alloy compared with the casting. Gianoglio et al. [27] showed that discontinuous eutectic structure is formed in the Al-3wt.%Er alloy fabricated by laser melted single track, and the hardness reaches 88 HV. In LPBF process, it has been found that the addition of 0.2 wt.% Er improves the strength of Al-Si alloy [28]. In addition, Al_3Er intermetallic was formed in Er-modified 7075

aluminum alloy, which can refine the grains and reduce the cracks [29]. Recently, a novel high-strength Er and Zr modified Al-Mn-Mg alloy has been manufactured by LPBF. The microstructure contains columnar grains with a small number of equiaxed grains at melt pool boundaries, and ultimate tensile strength reaches 502 MPa with an elongation of 12% [30]. However, there is no systematically detailed investigation on the mechanism of Er and Zr in aluminum during the LPBF process.

In order to reveal the mode of existence of Er and Zr elements in aluminum alloy and its mechanisms on microstructure and properties during rapid solidification, Al-0.88Er-0.78Zr (wt.%) alloy was fabricated by LPBF process. Meanwhile, the effect of direct aging treatment on the following properties (e.g, solid solubility, precipitation, grain size, hardness and conductivity, etc.) were investigated. Then, the formation and mechanism of secondary phase in this alloy were discussed.

2. Experimental methods

2.1 Powder and samples preparation

The Al-0.88Er-0.78Zr (wt.%) alloy powder used in this study was prepared by vacuum induction melting inert gas atomization method (VIGA) under high gas pressure (3.2 MPa). The preparation process was performed under high-purity argon atmosphere, and argon gas was used as the inert gas. The gas flow rate was about 1200 m^3/h. After the preparation process, the Al-Er-Zr alloy powder was extracted from the collection chamber. The chemical compositions of the raw powder were determined by inductively coupled plasma atomic emission spectroscopy (ICP-AES), as shown in Table 1. Shown in Fig. 1 is morphology of the powder. The particle size distribution of the powder ranged from 20-58 μm, with a mean particle diameter d_{50}=41 μm.

Table 1. Chemical compositions of the Al-Er-Zr alloy determined by ICP-AES (wt.%).

Alloy element	Al	Er	Zr	Fe	Mg	Cu
Al-Er-Zr	Balance	0.88	0.78	0.03	0.14	0.01

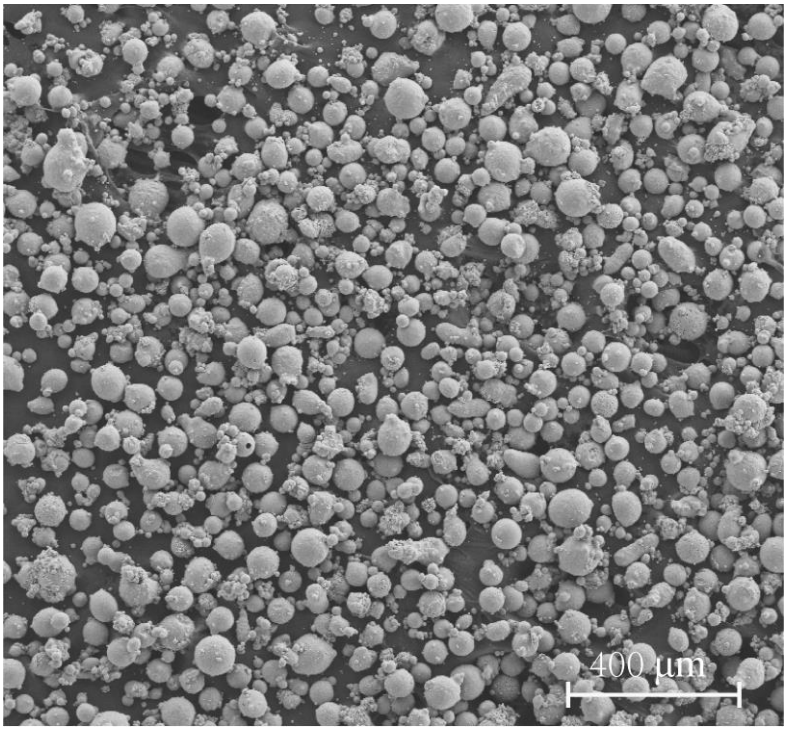

Fig. 1. Secondary electron image showing the morphology of the Al–Er-Zr alloy powder.

First of all, the powder was dried in a vacuum drying box for 10 hours at 120 ℃. LPBF process was conducted in a M280 powder-bed machine (SLM solutions, Germany), which consisted of a 400 W fiber laser operating in continuous mode at a wavelength of 1070 nm and a spot size of 80 μm. During the LPBF, high purity argon was filled into the forming cavity to prevent oxidation. The preheating temperature was set at 150 ℃, and powder layer thickness was fixed at 30 μm. Cubic samples, with dimensions of 10 mm ×10 mm ×10 mm, were fabricated by using the process parameters of laser power (P=350 W), scanning speed (v=1500 mm/s), hatch distance (h=0.13 mm) and an alternating scan strategy shown in Fig. 2a. The microstructure in XY-plane and XZ-plane (Fig. 2b) were observed.

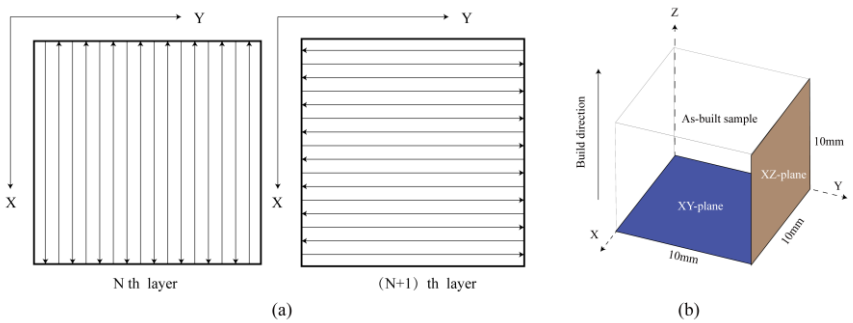

Fig. 2. (a) Schematic diagram of scanning strategy on the XY-plane; (b)Sectional planes of LPBF samples for microstructural observation.

2.2 Microstructure characterization

The as-built samples were polished according to normal metallographic method to a mirror-like finish, then were etched with HF (1 mL) + HCl (1.5 mL) + HNO_3 (2.5 mL) and deionized water (95 mL) for 15 s. The microstructure was characterized, using optical microscopy (OM, Olympus DP72, Japan) and scanning electron microscopy instrument (SEM, FEI Quanta 650FEG, USA) equipped with energy-dispersive X-ray spectroscopy (EDX) and electron backscattered diffraction (EBSD) systems. EBSD samples were electropolished using a struers electrolytic instrument (LectroPol-5, Denmark), at the voltage of 20 V for 15 s. The EBSD maps were recorded at the step size of 0.3 μm or 0.5 μm, and the HKL CHANNEL5 software was used to analyze the crystallographic orientation and grain size. Thin foils for TEM observation were prepared by twin-jet polishing (Struer TenuPol-2), using a 15 V constant voltage at -25 ℃. The intermetallic was characterized using transmission electron microscopy (TEM, JEOL JEM2100F, Japan) system operating at 200 KV and equipped with selected area electron diffraction (SAED) apparatus. EDX analysis was performed in scanning transmission electron microscopy mode (STEM). The concentration of Er and Zr in the matrix before and after heat treatment was measured using STEM-EDX point scan in the matrix without precipitates. Five points were measured, and the average was taken as the final result and error bars were calculated. The phase size was measured by Image J software.

2.3 Tests of mechanical properties

The isochronal aging treatment was conducted in air circulation furnace (KSL-1200X-J, China) from 200 °C, terminating at 550 °C, with increments of 25 °C, each lasting 3 hours. After aging, samples were taken out for water quenching treatment. After surface grinding and polishing, the hardness of XZ-plane was measured by vickers hardness tester (hxd-1000tm / LCD), using a load of 200 g and a holding time of 10 s. The average value and standard deviation of 8 different points were calculated as the final hardness. The electrical conductivity (EC) of the XZ-plane was measured five times, using a Foerster SIGMATEST 2.069 eddy current device at room temperature.

3. Results

3.1 As-built sample microstructure

3.1.1 Equiaxed-columnar bimodal grain structure

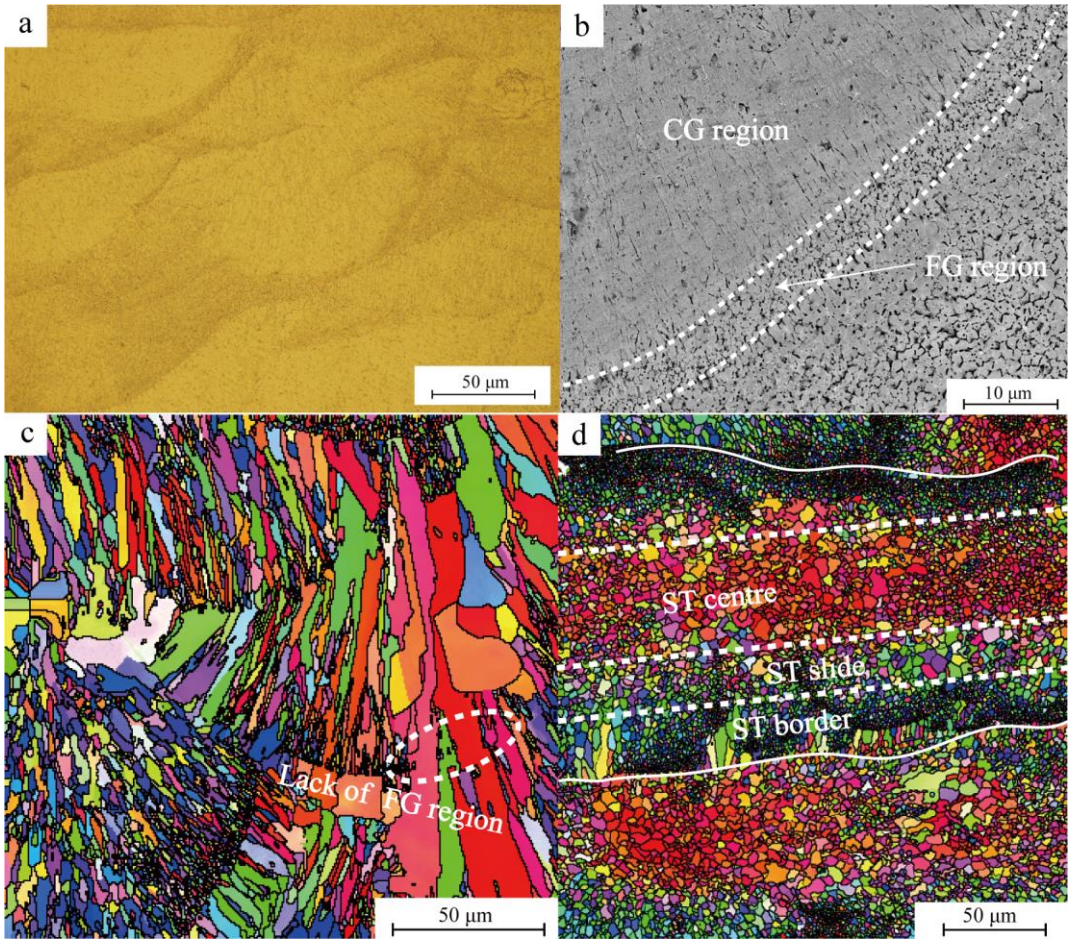

Fig. 3. Bimodal grain structure in as-built sample: (a) Low magnification optical microscope microstructure of XZ-plane; (b) SEM secondary electron image of XZ-plane after corrosion; (c) EBSD map of XZ-plane; (d) EBSD map of XY-plane.

Morphology and distribution of the molten pool in as-built samples is presented in Fig. 3a. The center and boundary of the molten pool consist of grains with different morphologies. The microstructure of XZ-plane, observed by SEM after corrosion, is shown in Fig. 3b. Bimodal grain structure, composed of fine equiaxed grains (FG region) at the molten pool boundary and coarse columnar grains (CG region) in the inner area of the molten pool, is obtained, which is similar to Sc-Zr modified aluminum alloy [31, 32]. EBSD image of XZ-plane (Fig. 3c) also confirms the existence of the bimodal grain structure. It is found that columnar grains are significantly refined and have no orientation relationship with each other, where equiaxed grains are distributed at the molten pool boundary. Conversely, when equiaxed grains are absent at the molten pool boundary, the large size columnar grains show epitaxial growth from one molten pool to another along the [001] orientation [4]. The statistics result of grain width in EBSD image shows that the average grain width of the as-built samples in Al-Er-Zr

alloy is 2.09 μm (columnar grain width ~2.57±0.84 μm), which is one tenth of the columnar grain size in laser remelted Al-Er-Zr alloy [26], and one fifth of the columnar grain size in Al-Si alloy fabricated by LPBF [5].

Equiaxed grain structure in EBSD image of XY-plane is presented in Fig. 3d, which is attributed to the different observation of grain cross-section. The scanning tracks (ST) can be seen in XY-plane, and the width of ST is about 129 μm, which is equal to the hatch distance. The grain size in ST center is equivalent to the ST slide, but they are larger than the grain size in ST border. The grain orientation in ST center is mostly along the [001] direction, while grains in ST slide and ST border show no obvious preferred orientation. This suggests that columnar grains (distributed in the ST center and ST slide) present different growth methods. The columnar grains in the ST center grow mainly by epitaxial growth, while grains in ST slide grow by competitive growth [4]. Fine equiaxed grains with different orientation are distributed in the ST border.

3.1.2 Intermetallic in microstructure

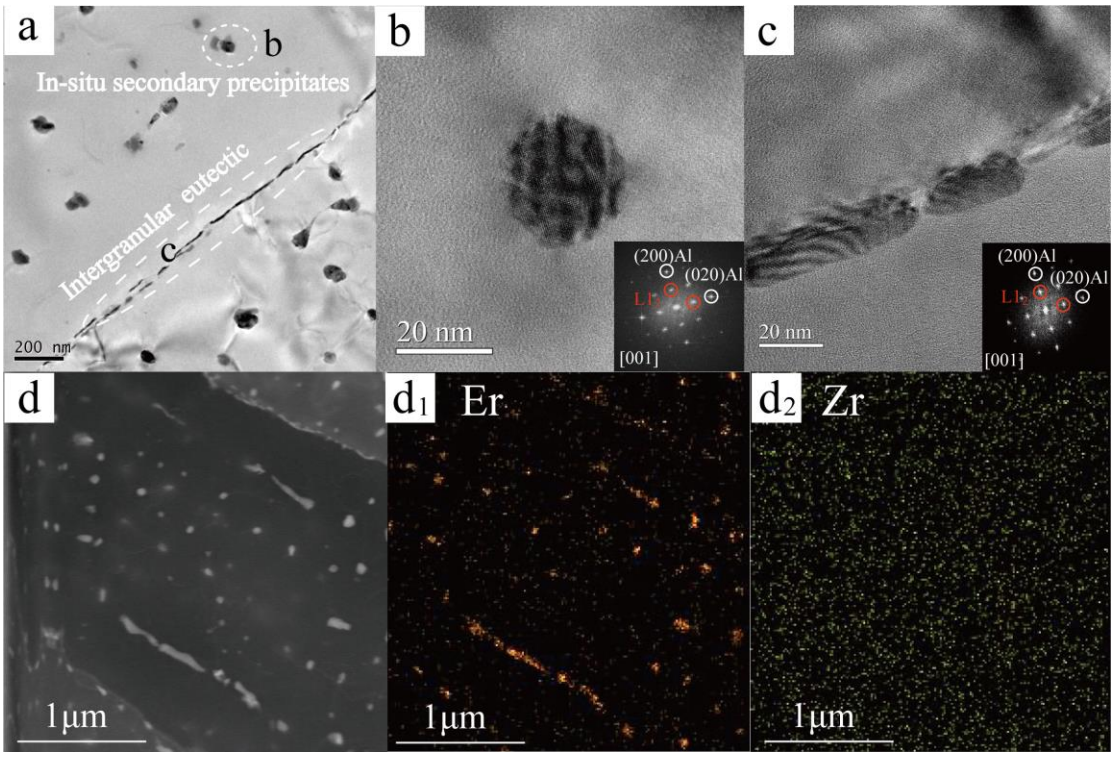

Fig. 4. TEM images of columnar grain structure: (a) Low magnification BF-TEM image showing in-situ secondary precipitates and intergranular eutectic distributed in columnar grains; (b) In-situ secondary precipitates; (c) Eutectic particles distributed at the grain boundary (The inset images in (b) and (c) showing $L1_2$ superlattice structure along [001] zone axis under FFT patterns corresponding to the precipitates and Al

matrix); (d) STEM-EDX mapping image in columnar grains showing that Er-rich particles are distributed in the grain and at the grain boundary.

In order to analyze the intermetallic in bimodal grain structure, the columnar and equiaxed grain structures were observed by TEM. First, intermetallics are observed in columnar grain and at grain boundary (Fig. 4a). The particles in columnar grain with spherical shape and size of 28.79 ± 2.96 nm, present $L1_2$ superlattice structure, as shown in Fig. 4b. Meanwhile, the $L1_2$ structured particles are also found at the grain boundary, showing a short rod-like shape (Fig. 4c). The result of STEM-EDX mapping displays that all particles are mainly enriched in Er atoms, and Zr atoms are uniformly distributed in the matrix (Fig. 4d). Hence, the particles in columnar grain may be in-situ secondary Al_3Er or $Al_3(Er,Zr)$ precipitates with $L1_2$ structure, produced by the action of thermal cycling. Similar results have been reported in the LPBF-processed Al-Mg-Sc-Zr alloy with low laser scanning speed [33], and in the laser-directed energy deposition (L-DED) processed Al-Mg-Sc-Zr alloy [34]. The Er-rich particles are also found at the grain boundary, which are considered to be the Al_3Er particles formed by the eutectic reaction in the later stage of solidification [35].

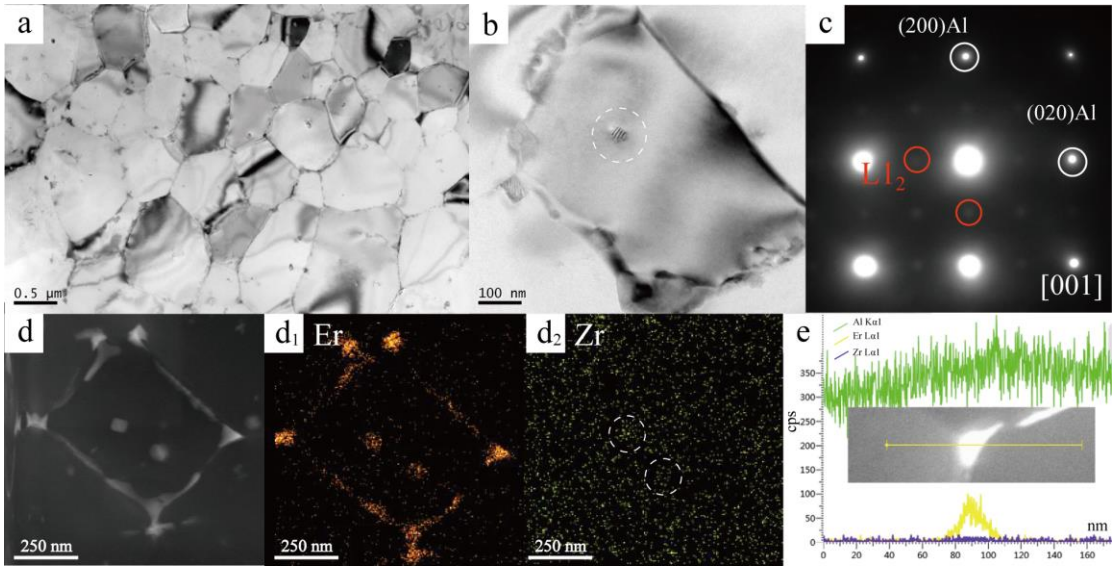

Fig. 5. TEM images of equiaxed grain structure: (a) Low magnification BF-TEM image taken from the fine-grain region; (b) heterogeneous nucleation particle found in fine equiaxed grain (highlighted by a white circle); (c) SAED pattern along [001] zone axis taken from the particle circled in Fig. 5b; (d) STEM-EDX mapping images in equiaxed grain; (e) STEM-EDX line scan across the equiaxed grain boundary.

A large number of equiaxed grains with average size of ~ 0.53 ± 0.15 μm are found at the boundary of the molten pool, as shown in Fig. 5a. It can be also found that there is

a particle with size of ~ 30.10 ± 4.58 nm distributed in the equiaxed grain (Fig. 5b). The SAED result reveals that the particle has $L1_2$ superlattice structure (Fig. 5c). STEM-EDX mapping images in equiaxed grain are shown in Fig. 5d. It shows that these particles in equiaxed grain are enriched in abundant Er element and little Zr element. Therefore, it is reasonable to assume that these Al_3(Er,Zr) particles act as the heterogeneous nucleation sites to form equiaxed grains, which refines the grain size [10, 12]. From the Fig. 5d1, it can be found that Er elements are also enriched at the grain boundary, but the enrichment of Zr element is not found. This is consistent with the results of EDX-line scan across the phase at the grain boundary (Fig. 5e). It is believed that eutectic Al_3Er particles are formed at the grain boundary [36].

The solute concentration in bimodal grain structure was tested by STEM-EDX points scanning, and the result shows that the concentration of Er and Zr in the equiaxed grains is relatively low, respectively 0.35 ± 0.13 wt.% and 0.59 ± 0.1 wt.%, while they are relatively high in the columnar grains, respectively 0.61 ± 0.13 wt.% and 0.77 ± 0.19 wt.% (Table 2). Therefore, Er and Zr elements have the tendency to precipitate during the heat treatment.

Table 2. The concentration of Er and Zr in bimodal grain structure

Bimodal grain structure	Er（wt.%）	Zr（wt.%）
columnar grains	0.61±0.13	0.77±0.19
equiaxed grains	0.35±0.13	0.59±0.1

3.2 Direct aging treatment

3.2.1 Hardness and electrical conductivity evolution

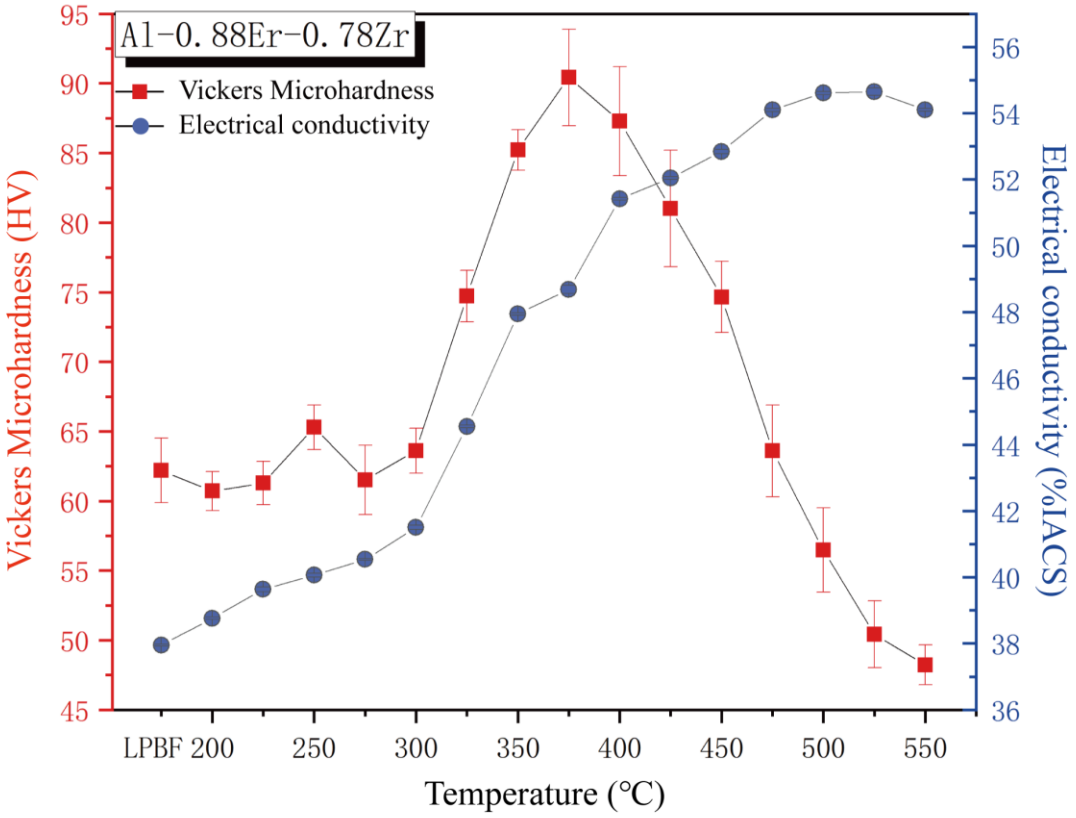

Fig. 6. Hardness and electrical conductivity curves of Al-Er-Zr alloy after isochronal aging treatment.

Table 3. The concentration of Er and Zr in columnar grains before and after aging treatment.

Aging states	Er（wt.%）	Zr（wt.%）
As-built sample	0.61±0.13	0.77±0.19
375℃ peak-aging	0.13±0.12	0.63±0.18
500℃ over-aging	0.1±0.14	0.16±0.11

Hardness and electrical conductivity curves of Al-Er-Zr alloy during 200-550 ℃ isochronal aging with increments of 25 ℃ each lasting 3 hours are shown in Fig. 6. The hardness curve presents a trend of increasing first and then decreasing. The hardness of the as-built sample is 62.22±2.61 HV. After 375 ℃/3 h aging treatment, the peak hardness reaches 89.24±3.77 HV. It should be pointed out that the trend of electrical conductivity (EC) with aging temperature is different from hardness. The EC increases gradually before 500 ℃, and remains relatively stable in the temperature range of 500-525 ℃. It begins to reduce after 525 ℃. For dense materials, it has been found that EC is mainly determined by the content of solute in the matrix [37, 38].

The concentration of solute elements in columnar grains before and after aging

treatment are listed in Table 3. The content of Er and Zr is reduced during the peak aging, indicating the precipitation of Er and little Zr at this temperature, which leads to the increase of EC and hardness. Compared with the 375 ℃/3 h peak aging, the solute content of Er during 500 ℃/3 h aging treatment not changes significantly, but the content of Zr greatly reduces from 0.63 wt.% to 0.16 wt.%, which may further improve the EC. The concentration of Er and Zr in the matrix is very low during 500 ℃ aging treatment. Therefore, further enhancement of aging temperature may not separate out more solute atom, but may promote the dissolution of secondary phases, resulting in the decrease of EC.

3.2.2 Effect of aging temperature on precipitates

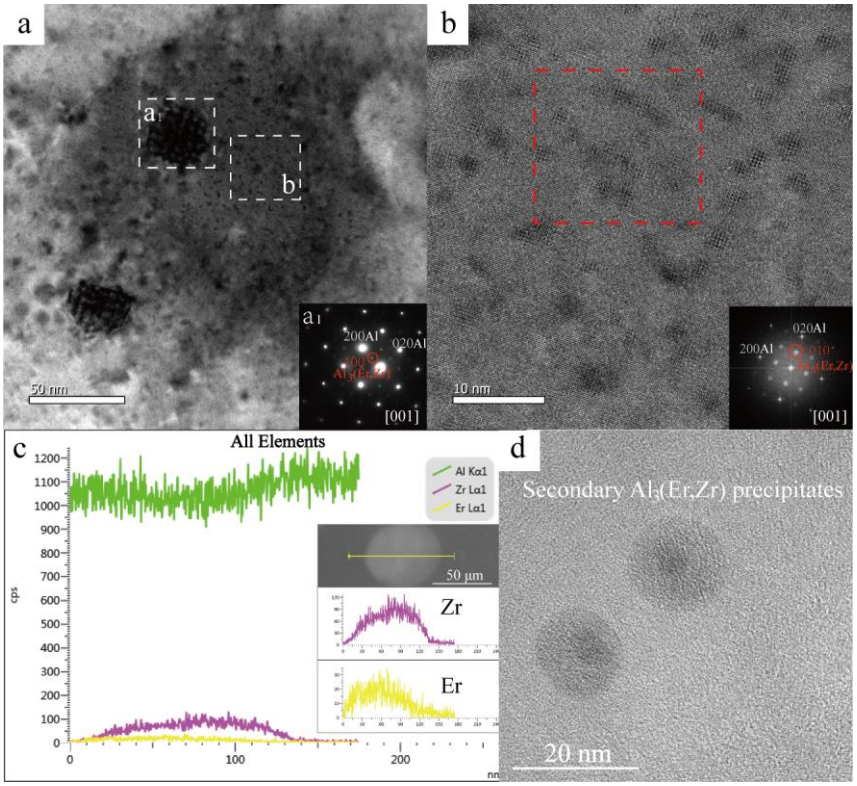

Fig. 7. Analysis of $Al_3(Er,Zr)$ precipitates at different aging temperatures: (a) Two sizes of $Al_3(Er,Zr)$ precipitates at 375 ℃ peak aging; (b) Secondary $Al_3(Er,Zr)$ precipitates at 375 ℃ aging treatment; (c) EDX line scan image of in-situ secondary $Al_3(Er,Zr)$ precipitate at 500 ℃ over aging; (d) Secondary $Al_3(Er,Zr)$ precipitates after 500 ℃ aging treatment.

There are two kinds of precipitation particles with different size in the columnar grains after 375 ℃/3 h peak aging (Fig. 7a). One is in-situ secondary $Al_3(Er,Zr)$ precipitates that are coarsened to ~ 31.32 ± 1.18 nm, and have $L1_2$ superlattice structure (Fig. $7a_1$). The other is a large number of secondary precipitates with smaller size

(d=2.25 ± 0.3 nm), and also have $L1_2$ superlattice structure after Fast Fourier Transform (FFT) (Fig. 7b). In combination with the precipitation of Er and Zr elements after peak aging (Table 3), it is reasonable to infer that these particles, presented dispersion distribution and coherent with the matrix, are secondary Al_3(Er,Zr) precipitates, which plays a major role in enhancing the hardness. After 500 ℃/3 h over aging, the in-situ secondary precipitates are further coarsened to ~58.54 ± 7.84 nm, due to the precipitation of Zr element. The result of EDX line scan suggests that in-situ secondary precipitates are mainly enriched in Er and Zr elements, and the signal intensity of the Zr element exceeds the Er element (Fig. 7c). Meanwhile, The size of the secondary Al_3(Er,Zr) precipitates in the columnar grains is coarsened to ~13.2 ± 1.88 nm (Fig. 7d). Due to the enrichment of Zr element, the core and shell of these precipitates present contrast differences.

3.2.3 Effect of aging treatment on grain size

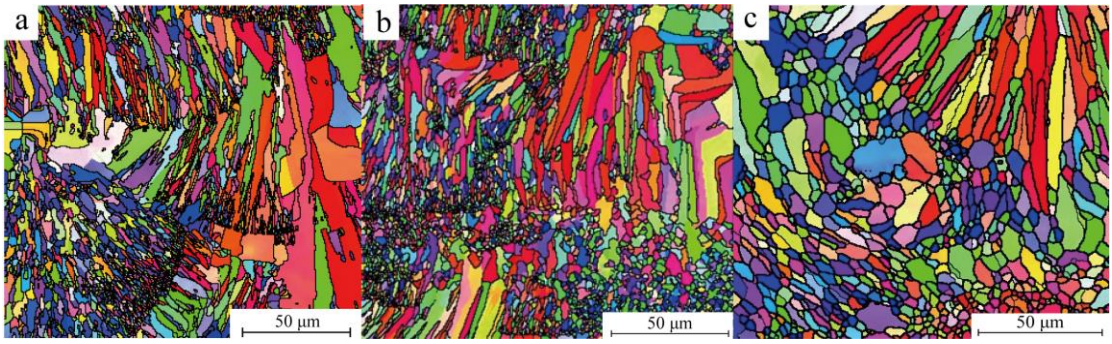

Fig. 8. EBSD images in different aging treatment states: (a) As-built; (b) 375 ℃/3 h peak aging; (c) 500 ℃/3 h over aging.

In order to study the effect of aging temperature on grain size, the as-built, 375 ℃/3 h peak aging and 500 ℃/3 h over aging samples were observed by EBSD (Fig. 8). In as-built and 375 ℃/3 h peak aging samples, the grain size not changes significantly. However, the grain size is obviously coarsened after 500 ℃/3 h over aging. The statistical result shows that the size of columnar grains width is coarsened to 3.84 ± 1.07 μm, and the size of equiaxed grains is coarsened to 2.78 ± 0.64 μm. Therefore, equiaxed grains have a higher coarsening rate than columnar grains.

4. Discussion

4.1 Mode of existence of Er and Zr

4.1.1 Solid solution in the matrix

Due to the large atomic radius, the solid solubility of rare earth elements in Al is very low. The atomic radius of Er is 0.1757 nm, which is 23% bigger than that of Al. According to the Hume-Rothery rule [39], when the difference of the atomic radius between solute and solvent is greater than 15%, a small solid solubility would be formed in the alloy. Therefore, the solid solubility of Er in Al in equilibrium condition is only about 0.05 wt.% [40]. Chilling condition of metal mold casting increases the solid solubility of Er, but generally it will not exceed 0.2 wt.% [35]. LPBF process has higher cooling rate (up to 10^{3-6} K/s [2]) than metal mold casting, which could increase solid solubility of Er. However, it has been reported that solid solubility of Er decreases by 0.0038 at% with the increasing of 0.01 at% Zr [41]. Therefore, the solid solubility of Er in the columnar grains reaches 0.61 ± 0.13 wt.% (Table 2) under the influence of above factors in this work. Griffiths et al. [7] proved that the solid solubility of Zr in the columnar grains could reach 1.5 wt.% in Al-Mg-Zr alloy fabricated by LPBF. The solid solubility of Zr in this study reaches 0.77 ± 0.19 wt.%, which reveals that Zr atoms are completely dissolved in the columnar grains. Simultaneously, the solid solubility of Er and Zr in the columnar grains are higher than that in the equiaxed grains (Table. 2). This difference is mainly controlled by the solidification process. On the one hand, from the low-temperature semi-solid remelting zone at the molten pool boundary to the high-temperature liquid zone in the inner region of the molten pool, the temperature of liquid phase gradually increases [33], leading to the increase of the solubility of Er and Zr elements in liquid phase. On the other hand, from the boundary to the center in molten pool, the solidification velocities increase, resulting in more solute elements trapped in the fcc-Al grains [7]. Wang et al. [42] also verified by numerical simulation that the cooling rate from boundary to center in molten pool would gradually increase. Therefore, columnar grains at the inner region of the molten pool have higher solute concentration of Er and Zr elements than equiaxed grains at the molten pool boundary.

4.1.2 In-situ secondary precipitates

First of all, the origin of in-situ secondary precipitates is discussed combining with the characteristics of LPBF process. According to the classical nucleation theory [43], the unit volume phase transition free energy $\triangle G_v$ is the chemical driving force for the phase transition. The $\triangle G_v$ is identified as:

$$\Delta G_v = (\frac{RT}{V_m}) X_\beta \ln(C_e/C_0)$$

Where R is the gas constant, T is the absolute temperature, V_m is the mole volume of the secondary phase, X_β is the atomic concentration of the solute in the secondary phase, C_e and C_0 are the concentrations of the solute in the equilibrium state and supersaturated state, respectively. With the increase in supersaturated solid solubility of solutes, the absolute value of $\triangle G_v$, the chemical driving force for phase transition, increases gradually. When the molten pool is just solidified, the solute concentration of Er in the matrix may exceed 0.61 wt.%. However, the solid solubility of Er in the equilibrium state is extremely low (less than 0.05 wt.%), which may provide a large driving force for the nucleation of Al_3Er or $Al_3(Er,Zr)$ particles. Moreover, the unique thermal cycling phenomenon in LPBF process could provide thermodynamic conditions for the nucleation and growth of in-situ secondary precipitates. The schematics are illustrated in Fig. 9. When the scanning track in Nth layer is formed by laser, the temperature of the molten pool in this scanning track is very high (Fig. 9b), which would produce heat input to the molten pool A shown in Fig. 9a. On the other hand, With the increase of layers, local preheating temperature of the solidified molten pool A would be enhanced by the continuous heat input from the post-forming layers (Fig. 9c). In the combined action of thermal cycling and the chemical driving force of supersaturated solute atoms, in-situ secondary Al_3Er or $Al_3(Er,Zr)$ precipitates with large size and small quantity are formed (Fig. 9d-e). Wang et al. [34] revealed that the temperature of solidified layer in Al-Mg-Sc-Zr alloy fabricated by laser directed energy deposition (L-DED) is kept at 325 ℃ for a long time under the action of thermal cycle, which promotes the coarsening of in-situ secondary $Al_3(Sc,Zr)$ precipitates up to ~ 20 nm. However, when the substrate is cooled by water during forming process, the thermal cycle condition would be changed, and the formation of in-situ secondary precipitates is also inhibited. It has been found that the diffusion coefficient (D) of Er is larger than that of Sc at 300 ℃ [17]. The critical radius of Al_3Er particles from coherent

to semi-coherent is ~8-9 nm [20], which is smaller than the size of in-situ secondary precipitates in this work. Fig. 9(f) shows the dislocations around these particles. In the classical coherent/semi-coherent transition theory, dislocations will appear at the particles after the semi-coherent transition, indicating that the particles get into a semi-coherent state [44]. The coarsening rate may change when the coherent relationship between precipitates and matrix is vanished. For example, when $Al_3(Sc,Zr)$ particles lose the coherent relationship with matrix in Al-Sc-Zr alloy, the interfacial energy and the coarsening rate of the precipitates increase [45]. Therefore, in this work, the semi-coherent in-situ secondary precipitates grow rapidly and form a size of 28.79 ± 2.96 nm.

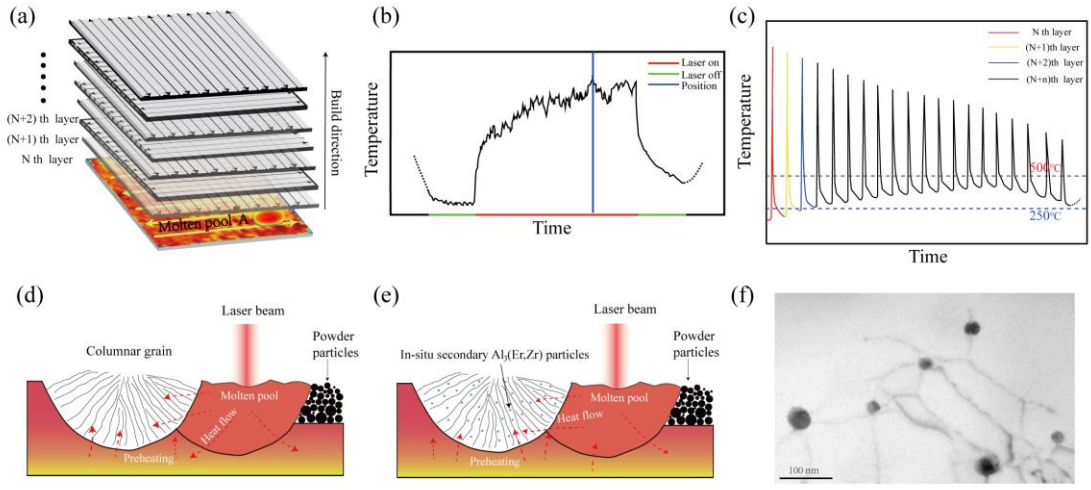

Fig. 9. The effect of thermal cycling on the formation of in-situ secondary precipitates: (a) Schematic of laser layered scanning; (b) Schematic of temperature distribution curve around the molten pool A in a scanning track; (c) Schematic of temperature change curve of molten pool A during the laser forming different layers; (d) and (e) Schematics of thermal cycling promoting the formation of in-situ secondary precipitates; (f) Dislocations existing around the in-situ secondary precipitates.

4.1.3 Grain boundary eutectic particles

As shown in Fig. 4d and Fig. 5d, the enrichment of Er is found at the columnar and equiaxed grain boundaries in as-built samples. It is reasonable to assume that a binary eutectic reaction occurs to form Al_3Er intermetallic. From the equilibrium phase diagram (Fig. 10), the addition of Er in this work reaches 0.88 wt.% (0.15 at%), which belongs to hypoeutectic composition. The solute partition coefficient (k) of Er in Al-Er binary phase diagram is far less than unity. Therefore, during solidification Er atoms are accumulated at the front of the interface between solid and liquid. When the

Er concentration approaches the eutectic point, Al_3Er will form by the decomposing eutectic reaction. It also has been found that when the Er concentration reaches 0.4 wt.% in casting, the eutectic Al_3Er particles are observed at the grain boundaries [35]. The eutectic Al_3Er intermetallic distributed at the grain boundary can hinder the grain boundary migration and grain growth, which will be discussed in detail later.

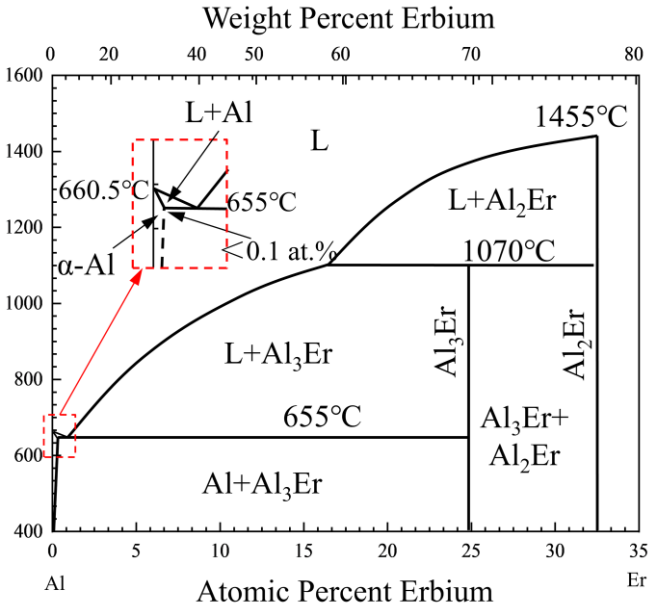

Fig. 10 Al-Er binary phase diagram.

4.2 Mechanisms of Er and Zr

4.2.1 Forming a bimodal grain structure

The TEM image (Fig. 5b) presents that $Al_3(Er,Zr)$ heterogeneous nucleation particles are observed in fine equiaxed grains. One of the important sources of heterogeneous nucleation particles may contain the in-situ secondary Al_3Er or $Al_3(Er,Zr)$ precipitates in the columnar grains that are not completely melted during remelting process. This is because the particle size in FG-region and CG-region are almost same. On the other hand, it is determined by the remelting characteristics of the layer-by-layer in LPBF process. When the Nth layer is formed by laser, powder of this layer will be melted. In addition, former solidified layers will also be remelted to realize the metallurgical bonding between layers [32]. The remelting zone is mainly composed of the CG-regions with in-situ secondary precipitates. Spierings et al. [32] demonstrated that the temperature in molten pool center is high, but the temperature in the molten pool boundary is low (only 635-800 ℃) in the Al-Mg-Sc-Zr alloy fabricated by LPBF. However, the melting point of Al_3Er phase is about 1070 ℃ [27]. Therefore, it could be inferred that in the remelting zone at the molten pool boundary, in-situ

secondary Al_3Er or $Al_3(Er,Zr)$ precipitates will not be completely melted (Fig. 11a). The lattice constant of the Al_3Er phase ($L1_2$ superlattice structure) is 0.4215 nm, which is close to lattice constant of the matrix Al (face-centered cubic structure, a=0.4049 nm), and only 4.08% lattice mismatch with the aluminum matrix [46]. When Zr atoms are precipitated around Al_3Er particles, the lattice mismatch can be further reduced (Al_3Er ~4.08%, $Al_3(Er,Zr)$ ~0.75% [47]). Hence, the unmelted in-situ secondary particles at the molten pool boundary could act as the sites for heterogeneous nucleation, promoting the formation of fine equiaxed grain (Fig. 11b). In addition to the in-situ secondary precipitates, the eutectic Al_3Er particles at the grain boundary may also not be completely melted during remelting process, promoting the formation of equiaxed grains [14]. In the study of laser remelting Al-3.43Er-0.13Zr (wt.%) substrate, a large number of in-situ secondary $Al_3(Er,Zr)$ particles are also found in the laser melting zone, but only coarse columnar grains are obtained [26]. This may be because the process of laser remelting substrate is different from LPBF and only involves once melting and solidification of the surface layer. Consequently, the formed in-situ secondary precipitates have no chance to act as the sites for heterogeneous nucleation, which shows the limitation of laser remelting in development of new materials.

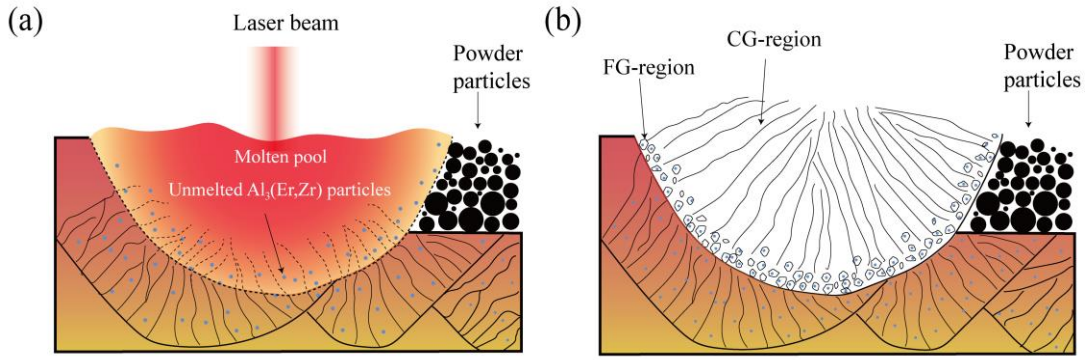

Fig. 11. Schematics of the formation of FG region at the molten pool boundary: (a) Part of the in-situ secondary precipitates at the molten pool boundary are not completely melted when laser is forming the next layer; (b) Unmelted $Al_3(Er,Zr)$ particles serve as heterogeneous nucleation sites to form the fine equiaxed grain region（FG region）at the boundary of the molten pool.

From the boundary of the molten pool to the center, the temperature gradient (G) gradually decreases, while the solidification velocity (R) gradually increases [42]. Although the columnar grain tends to be formed in the case of high G/R value [4], unmelted heterogeneous nucleation particles at the molten pool boundary could

overcome the high G/R value to promote the formation of equiaxed grains [14]. Temperature gradient in the molten pool center could reach a high level of 10^{6-7} K/m [48], and the potentially Al_3Er or $Al_3(Er,Zr)$ heterogeneous nucleation particles are melted due to the high temperature in the molten pool center, leading to the columnar grain growth. Therefore, bimodal grain structure is formed in Al-Er-Zr alloy fabricated by LPBF. The formation of equiaxed grains at the molten pool boundary can refine the columnar grains size in molten pool center. This is because the continuous epitaxial growth of the columnar grains is blocked by the equiaxed grains distributed at grain boundary, which will reduce the long axis and width dimensions of the columnar grains [49]. Therefore, the overall grain size is refined.

4.2.2 Improving hardness of peak aging

In Al-Er alloy produced by cast, nano-Al_3Er precipitates exhibit a significant aging hardening behavior during the heat treatment，and the addition of Zr could further improve the peak hardness of Al-Er alloy [50]. It has been proved in Ref [23] that the Er elements with faster diffusion rate are precipitated to form the core of Al_3Er, which provides nucleation sites for the precipitation of Zr. Afterwards, the precipitation of Zr element can prevent the rapid coarsening of Al_3Er particles, stabilizing the number density and increasing the volume fraction of the precipitates. Therefore, the precipitation of $Al_3(Er,Zr)$ particles shows a synergistic effect and greatly improves the peak hardness in Al-Er-Zr alloy during the aging treatment. It can be seen from (Fig. 7b) that $Al_3(Er,Zr)$ particles are precipitated during 375 ℃/3 h aging treatment, which will be considered as the main reason for the increase of hardness. The nano-sized secondary $Al_3(Er,Zr)$ particles are interface coherence with the matrix, which is beneficial to improve the mechanical properties of the alloy. The strengthening effect of precipitates on the matrix is mainly achieved by hindering the dislocations movement. It could be divided into dislocation cutting and bowing precipitate mechanisms. Zhang et al. [20] found the critical diameter (about 4.8 nm) of dislocation cutting and bowing around Al_3Er particles. For the precipitates with a diameter < 4.8 nm, the dislocations mainly cut through the particles. In the initial stage of aging, the main strengthening mechanism is the sum of coherent strengthening and modulus strengthening. As the size of particles increases, the strengthening mechanism becomes order strengthening, and the peak hardness will be reached at this time [20]. Therefore, the strengthening mechanism of the secondary $Al_3(Er,Zr)$ precipitates with a diameter of 2.25 nm could

be ordered strengthening. When the size of the particles is larger than 4.8 nm, the strengthening mechanism changes to Orowan strengthening [20]. It suggests that the strengthening mechanism of in-situ secondary $Al_3(Er,Zr)$ precipitates with a diameter of 31.32 nm could be Orowan strengthening. Overall, it is considered that the peak hardness during 375 ℃/3 h aging treatment is the sum of grain boundary strengthening (caused by heterogeneous nucleation), solid solution strengthening, Orowan strengthening of in-situ secondary precipitates and order strengthening of nano-sized secondary $Al_3(Er,Zr)$ particles.

Table 4 lists the hardness values of alloys similar to Al-Er-Zr under different processes. It could be found that compared with the as-cast Al-Er-Zr alloy, LPBF process refines the grain size, and expands the supersaturated solute content of Er and Zr elements, which improves the hardness of as-built sample. Meanwhile, the high solute solid solubility promotes the dispersed precipitation of $Al_3(Er,Zr)$ particles during the aging treatment, increasing the hardness by 78% compared with the as-cast peak aging. In addition, Al-Er-Zr alloys have the highest hardness in as-built condition compared with Al-Sc-Zr alloys. The peak hardness of Al-Er-Zr alloy fabricated by LPBF after ageing treatment is comparable to that Al-Sc-Zr alloy in as-cast peak aging and lower than that Al-Sc-Zr alloy in the laser-melting peak aging. However, the price of Er is only 1/80 of that Sc. Er and Zr composite addition has significant cost advantages and is expected to become an additive for the development of low-cost and high-strength aluminum alloy.

Table 4. Comparison of hardness of alloys similar to Al-Er-Zr under different forming processes.

Alloy composition(wt.%)	Forming condition	As-built or as-cast hardness	Peak aging Hardness (HV)	Ref
Al-0.88Er-0.78Zr	LPBF	62	89	Our work
Al-3Er	Laser melted single track	88	-	[27]
Al-3.4Er-0.13Zr	Laser melting	77	88	[26]
Al-0.22Er-0.18Zr	Cast	26	50	[23]
Al-0.85Sc-0.18Zr	Laser melting	40	110	[26]
Al-0.85Sc-0.18Zr	Cast	50	90	[26]

4.2.3 Preventing grain growth

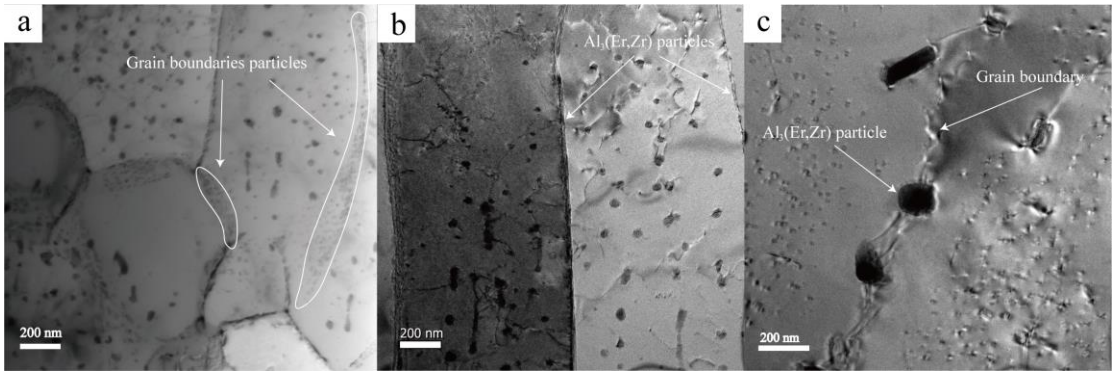

Fig. 12. Distribution of the grain boundaries $Al_3(Er,Zr)$ particles in different aging conditions: (a) As-built sample; (b) 375 ℃/3 h peak aging sample; (c) 500 ℃/3 h over aging sample.

It could be seen from Fig. 8 that the grain size of as-built sample hardly changes after aging at 375 ℃/3 h, but coarsens obviously at 500 ℃/3 h aging treatment. This is because the diffusion rate of atoms in matrix will enhance with increase of aging temperature, improving the driving force of grain boundary migration. The grain growth is controlled by grain boundary migration, but the dispersed fine secondary phase distributed at the grain boundary will hinder the grain boundary migration. It can be found from Fig. 12a that a large number of fine Al_3Er particles are distributed along the grain boundaries, which can pin dislocation, sub grain or grain boundary to prevent grain growth at high temperature [35, 41]. The resistance of dislocation migration can be described by Zener's formula [51]:

$$P_z = \frac{3}{4}\gamma\frac{f}{r}$$

P_z is the Zener force, which is the resistance of the secondary phase to dislocations and grain boundaries, γ is migration energy, f and r are the volume fraction and radius of the secondary phase particles, respectively. It could be seen that, the larger the volume fraction or the smaller the size of grain boundary particles, the greater the resistance of dislocations and grain boundary migration. In peak aging of 375 ℃/3 h, diffusion distance of Zr atoms is limited, which not leads to obvious coarsening of particles at the grain boundary. Furthermore, it is still distributed at the grain boundary in the form of small size and large quantity (Fig. 12b), providing a strong resistance to dislocation and grain boundary migration. Therefore, grain size is not coarsened during 375 ℃/3 h peak aging. According to Arrhenius equation, the diffusion coefficient of atoms increases exponentially with the temperature; the concentration of Zr in matrix decreases significantly during 500 ℃ /3 h over aging

(Table. 3). In addition, there are a large number of defects at the grain boundary. These defects are channels for solute elements diffusion, which promotes the precipitation of Zr, resulting in the serious coarsening of particles (particle size ~107.3 ± 14.86 nm) at the grain boundary. The coarsening of the secondary phases and the increasing of distance between adjacent particles at grain boundary (Fig. 12c) will weaken the resistance of grain growth, leading to the coarsening of grain size during 500 ℃ /3 h over aging.

5. Conclusion：

In this work, the microstructure and properties of Al-0.88Er-0.78Zr (wt.%) alloy fabricated by LPBF and subsequent direct aging treatment process were investigated; The mechanisms of Er and Zr were thoroughly discussed. The following major conclusions can be drawn:

- Bimodal grain structure, composed of fine equiaxed grain regions (~0.53 ± 0.15 μm) at the molten pool boundary and coarser columnar grain regions (columnar width ~2.57 ± 0.84 μm) at the molten pool center, is obtained in as-built samples.
- The LPBF process expands the supersaturated solid solubility of Er and Zr in the aluminum matrix, and Al_3Er particles are distributed at the grain boundaries in as-built samples. A large number of in-situ secondary Al_3Er or $Al_3(Er,Zr)$ particles are formed in columnar grains under the action of internal thermal cycle. These in-situ secondary precipitates and/or grain boundary eutectic particles may not be completely melted during remelting; they could act as the heterogeneous nucleation sites at the boundary of the molten pool, promoting the formation of equiaxed grains and refinement the grain size.
- After aging at 375 ℃ for 3 h, the peak hardness with a value of 89.24 ± 3.77 HV is reached. The precipitation of nano-sized $Al_3(Er,Zr)$ particles plays a major strengthening role. The distribution of grain boundary particles could inhibit the grain growth. Therefore, the grain size has not been coarsened during 375 ℃ /3 h peak aging.

Acknowledegments

This research was funded by National Key Research and Development Program of China (2021YFB3704205), General Program of Science and Technology

Development Project of Beijing Municipal Education Commission (KM 202110005010), Innovative Research Group Project of the National Natural Science Fund (Grant No. 51621003).

References

[1] N.T. Aboulkhair, M. Simonelli, L. Parry, I. Ashcroft, C. Tuck, R. Hague, 3D printing of Aluminium alloys: Additive Manufacturing of Aluminium alloys using selective laser melting, Progress in Materials Science, 106 (2019) 100578.
[2] J. Lewandowski, M. Seifi, Metal Additive Manufacturing: A Review of Mechanical Properties, Annual Review of Materials Research, 46 (2016) 151-186.
[3] W.E. Frazier, Metal Additive Manufacturing: A Review, Journal of Materials Engineering and Performance, 23 (2014) 1917-1928.
[4] L. Thijs, K. Kempen, J.-P. Kruth, J. Van Humbeeck, Fine-structured aluminium products with controllable texture by selective laser melting of pre-alloyed AlSi10Mg powder, Acta Materialia, 61 (2013) 1809-1819.
[5] H. Rao, S. Giet, K. Yang, X. Wu, C.H.J. Davies, The influence of processing parameters on aluminium alloy A357 manufactured by Selective Laser Melting, Materials & Design, 109 (2016) 334-346.
[6] J.H. Martin, B.D. Yahata, J.M. Hundley, J.A. Mayer, T.A. Schaedler, T.M. Pollock, 3D printing of high-strength aluminium alloys, Nature, 549 (2017) 365-369.
[7] S. Griffiths, M.D. Rossell, J. Croteau, N.Q. Vo, D.C. Dunand, C. Leinenbach, Effect of laser rescanning on the grain microstructure of a selective laser melted Al-Mg-Zr alloy, Materials Characterization, 143 (2018) 34-42.
[8] E. Ma, T. Zhu, Towards strength–ductility synergy through the design of heterogeneous nanostructures in metals, Materials Today, 20 (2017) 323-331.
[9] J.H. Martin, B. Yahata, J. Mayer, R. Mone, E. Stonkevitch, J. Miller, M.R. O'Masta, T. Schaedler, J. Hundley, P. Callahan, T. Pollock, Grain refinement mechanisms in additively manufactured nano-functionalized aluminum, Acta Materialia, 200 (2020) 1022-1037.
[10] M. Opprecht, J.-P. Garandet, G. Roux, C. Flament, M. Soulier, A solution to the hot cracking problem for aluminium alloys manufactured by laser beam melting, Acta Materialia, 197 (2020) 40-53.
[11] H. Zhang, H. Zhu, X. Nie, J. Yin, Z. Hu, X. Zeng, Effect of Zirconium addition on crack, microstructure and mechanical behavior of selective laser melted Al-Cu-Mg alloy, Scripta Materialia, 134 (2017) 6-10.
[12] J.R. Croteau, S. Griffiths, M.D. Rossell, C. Leinenbach, N.Q. Vo, Microstructure and mechanical properties of Al-Mg-Zr alloys processed by selective laser melting, Acta Materialia, 153 (2018) 35-44.
[13] S. Griffiths, J.R. Croteau, M.D. Rossell, R. Erni, A. De Luca, N.Q. Vo, D.C. Dunand, C. Leinenbach, Coarsening- and creep resistance of precipitation-strengthened Al–Mg–Zr alloys processed by selective laser melting, Acta Materialia, 188 (2020) 192-202.
[14] K.V. Yang, Y. Shi, F. Palm, X. Wu, P. Rometsch, Columnar to equiaxed transition in Al-Mg(-Sc)-Zr alloys produced by selective laser melting, Scripta Materialia, 145 (2018) 113-117.
[15] K.E. Knipling, D.N. Seidman, D.C. Dunand, Ambient- and high-temperature mechanical properties of isochronally aged Al–0.06Sc, Al–0.06Zr and Al–0.06Sc–

0.06Zr (at.%) alloys, Acta Materialia, 59 (2011) 943-954.
[16] A.B. Spierings, K. Dawson, K. Kern, F. Palm, K. Wegener, SLM-processed Sc- and Zr- modified Al-Mg alloy: Mechanical properties and microstructural effects of heat treatment, Materials Science and Engineering: A, 701 (2017) 264-273.
[17] Q. Jia, P. Rometsch, P. Kürnsteiner, Q. Chao, A. Huang, M. Weyland, L. Bourgeois, X. Wu, Selective laser melting of a high strength Al-Mn-Sc alloy: Alloy design and strengthening mechanisms, Acta Materialia, 171 (2019) 108-118.
[18] J. Bi, Z. Lei, Y. Chen, X. Chen, Z. Tian, X. Qin, J. Liang, X. Zhang, Effect of Al3(Sc, Zr) and Mg2Si precipitates on microstructure and tensile properties of selective laser melted Al-14.1Mg-0.47Si-0.31Sc-0.17Zr alloy, Intermetallics, 123 (2020) 106822.
[19] R. Li, M. Wang, Z. Li, P. Cao, T. Yuan, H. Zhu, Developing a high-strength Al-Mg-Si-Sc-Zr alloy for selective laser melting: Crack-inhibiting and multiple strengthening mechanisms, Acta Materialia, 193 (2020) 83-98.
[20] Y. Zhang, K. Gao, S. Wen, H. Huang, Z. Nie, D. Zhou, The study on the coarsening process and precipitation strengthening of Al3Er precipitate in Al–Er binary alloy, Journal of Alloys and Compounds, 610 (2014) 27-34.
[21] Z. Nie, T. Jin, J. Fu, G. Xu, J. Yang, J. Zhou, T. Zuo, Research on Rare Earth in Aluminum, Materials Science Forum, 396-402 (2002) 1731-1730.
[22] D. Xue, W. Wei, W. Shi, Y.W. Guo, S.P. Wen, X.L. Wu, H. Huang, Z.R. Nie, Effect of cold rolling on mechanical and corrosion properties of stabilized Al–Mg–Mn–Er–Zr alloy, Journal of Materials Research and Technology, 15 (2021) 6329-6339.
[23] S.P. Wen, K.Y. Gao, Y. Li, H. Huang, Z.R. Nie, Synergetic effect of Er and Zr on the precipitation hardening of Al–Er–Zr alloy, Scripta Materialia, 65 (2011) 592-595.
[24] M.E. van Dalen, R.A. Karnesky, J.R. Cabotaje, D.C. Dunand, D.N. Seidman, Erbium and ytterbium solubilities and diffusivities in aluminum as determined by nanoscale characterization of precipitates, Acta Materialia, 57 (2009) 4081-4089.
[25] J.H. Rao, Y. Zhang, X. Fang, Y. Chen, X. Wu, C.H.J. Davies, The origins for tensile properties of selective laser melted aluminium alloy A357, Additive Manufacturing, 17 (2017) 113-122.
[26] Q. Jia, P. Rometsch, S. Cao, K. Zhang, A. Huang, X. Wu, Characterisation of AlScZr and AlErZr alloys processed by rapid laser melting, Scripta Materialia, 151 (2018) 42-46.
[27] D. Gianoglio, S. Marola, L. Battezzati, A. Aversa, F. Bosio, M. Lombardi, D. Manfredi, M. Lorusso, Banded microstructures in rapidly solidified Al-3 wt% Er, Intermetallics, 119 (2020) 106724.
[28] Y.W. Guo, W. Wei, W. Shi, D. Xue, X.R. Zhou, S.P. Wen, X.L. Wu, K.Y. Gao, H. Huang, Z.R. Nie, Selective laser melting of Er modified AlSi7Mg alloy: Effect of processing parameters on forming quality, microstructure and mechanical properties, Materials Science and Engineering: A, 842 (2022) 143085.
[29] X. Zhang, Z. Xiao, W. Yu, C.K. Chua, L. Zhu, Z. Wang, P. Xue, S. Tan, Y. Wu, H. Zheng, Influence of erbium addition on the defects of selective laser-melted 7075 aluminium alloy, Virtual and Physical Prototyping, 17 (2022) 406-418.
[30] Y. Geng, C. Jia, J. Xu, Z. Zhang, H. Ju, D. Wang, L. Yu, Selective laser melting of a novel high-strength Er- and Zr-modified Al-Mn-Mg alloy, Materials Letters, 313 (2022) 131762.
[31] H. Zhang, D. Gu, J. Yang, D. Dai, T. Zhao, C. Hong, A. Gasser, R. Poprawe, Selective laser melting of rare earth element Sc modified aluminum alloy: Thermodynamics of precipitation behavior and its influence on mechanical properties, Additive Manufacturing, 23 (2018) 1-12.

[32] A.B. Spierings, K. Dawson, T. Heeling, P.J. Uggowitzer, R. Schäublin, F. Palm, K. Wegener, Microstructural features of Sc- and Zr-modified Al-Mg alloys processed by selective laser melting, Materials & Design, 115 (2017) 52-63.
[33] A.B. Spierings, K. Dawson, P.J. Uggowitzer, K. Wegener, Influence of SLM scan-speed on microstructure, precipitation of Al3Sc particles and mechanical properties in Sc- and Zr-modified Al-Mg alloys, Materials & Design, 140 (2018) 134-143.
[34] Z. Wang, X. Lin, N. Kang, J. Chen, Y. Tang, H. Tan, X. Yu, H. Yang, W. Huang, Directed energy deposition additive manufacturing of a Sc/Zr-modified Al–Mg alloy: Effect of thermal history on microstructural evolution and mechanical properties, Materials Science and Engineering: A, 802 (2021) 140606.
[35] S.P. Wen, Z.B. Xing, H. Huang, B.L. Li, W. Wang, Z.R. Nie, The effect of erbium on the microstructure and mechanical properties of Al-Mg-Mn-Zr alloy, Materials Science and Engineering: A, 516 (2009) 42-49.
[36] Z.M. Shi, Q. Wang, G. Zhao, R.Y. Zhang, Effects of erbium modification on the microstructure and mechanical properties of A356 aluminum alloys, Materials Science and Engineering: A, 626 (2015) 102-107.
[37] P.A. Rometsch, H. Zhong, K.M. Nairn, T. Jarvis, X. Wu, Characterization of a laser-fabricated hypereutectic Al–Sc alloy bar, Scripta Materialia, 87 (2014) 13-16.
[38] Y. Shi, P. Rometsch, K. Yang, F. Palm, X. Wu, Characterisation of a novel Sc and Zr modified Al–Mg alloy fabricated by selective laser melting, Materials Letters, 196 (2017) 347-350.
[39] M.L. Huggins, The Structure of Metals and Alloys (Hume-Rothery, William), Journal of Chemical Education, 13 (1936) 350.
[40] J.L. Murray, ASM handbook: alloy phase diagrams, ASM, 3 (1992) 226-290.
[41] C. Booth-Morrison, D.C. Dunand, D.N. Seidman, Coarsening resistance at 400 °C of precipitation-strengthened Al–Zr–Sc–Er alloys, Acta Materialia, 59 (2011) 7029-7042.
[42] Z. Wang, X. Lin, Y. Tang, N. Kang, X. Gao, S. Shi, W. Huang, Laser-based directed energy deposition of novel Sc/Zr-modified Al-Mg alloys: columnar-to-equiaxed transition and aging hardening behavior, Journal of Materials Science & Technology, 69 (2021) 168-179.
[43] A. Borisenko, Revision of the classical nucleation theory for supersaturated solutions, Physics, (2015).
[44] S. Iwamura, Y. Miura, Loss in coherency and coarsening behavior of Al3Sc precipitates, Acta Materialia, 52 (2004) 591-600.
[45] W. Jesser, On the theory of loss of coherency by spherical precipitates, Philosophical Magazine, 19 (1969) 993-999.
[46] K. Knipling, D. Dunand, D. Seidman, Criteria for developing castable, creep-resistant aluminum-based alloys – A review, Zeitschrift für Metallkunde, 97 (2006) 246-265.
[47] S.P. Wen, K.Y. Gao, H. Huang, W. Wang, Z.R. Nie, Precipitation evolution in Al–Er–Zr alloys during aging at elevated temperature, Journal of Alloys Compounds, 574 (2013) 92-97.
[48] Y. Li, D. Gu, Thermal behavior during selective laser melting of commercially pure titanium powder: Numerical simulation and experimental study, Additive Manufacturing, 1-4 (2014) 99-109.
[49] M. Opprecht, J.-P. Garandet, G. Roux, C. Flament, An understanding of duplex microstructures encountered during high strength aluminium alloy laser beam melting processing, Acta Materialia, 215 (2021) 117024.

[50] H. Huang, S. Wen, K. Gao, W. Wang, Z. Nie, Age Hardening Behavior and Corresponding Microstructure of Dilute Al-Er-Zr Alloys, Metallurgical and Materials Transactions A, 44 (2013).
[51] E. Nes, N. Ryum, O. Hunderi, On the Zener drag, Acta Metallurgica, 33 (1985) 11-22.

Graphical abstract